Research Square

Preprints are preliminary reports that have not undergone peer review.
They should not be considered conclusive, used to inform clinical practice,
or referenced by the media as validated information.

Vinca rosea-Derived Ag–ZnO Nanoparticles: Synthesis and Multifunctional Biological Applications in Cytotoxicity, Antidiabetic Activity, Antimicrobial Activity, and Dental Biofilm Control

Venkattappan Anbazhagan

anbu80@gmail.com

Department of Chemistry, Vinayaka Mission's Kirupananda Variyar Arts and Science College, Vinayaka Mission's Research Foundation

Senthilkumar Chandrasekaran

Department of Chemistry, Vinayaka Mission's Kirupananda Variyar Arts and Science College, Vinayaka Mission's Research Foundation

Surendiran Mohan

Department of Humanities and Sciences-Chemistry, Centre for Nanotechnology Research, Aarupadai Veedu Institute of Technology, Vinayaka Mission's Research Foundation (DU), Paiyanoor

A. Alvin Kalicharan

Department of Chemistry, Panimalar Engineering College (Autonomous), Poonamallee

Sherlin Joseph

Centre for Advanced Functional Materials, Chennai Institute of Technology

Shanmugam Anusuya

Department of Pharmaceutical Engineering, Vinayaka Mission's Kirupananda Variyar Engineering College, Vinayaka Mission's Research Foundation (Deemed to be University)

Sudheshkannan Rajendran

Novitium Pharma LLC (ANI Pharmaceuticals), 70 Lake Drive, East Windsor

Research Article

Keywords: Green synthesis, Vincarosea (L), antidiabetic, cytotoxic effect, biofilm

Posted Date: November 19th, 2026

DOI: https://doi.org/10.21203/rs.3.rs-11450466/v1

License: This work is licensed under a Creative Commons Attribution 4.0 International License.
Read Full License

Additional Declarations: No competing interests reported.

Vinca rosea-Derived Ag–ZnO Nanoparticles: Synthesis and Multifunctional Biological Applications in Cytotoxicity, Antidiabetic Activity, Antimicrobial Activity, and Dental Biofilm Control

Venkattappan Anbazhagan[1*], Senthilkumar Chandrasekaran[1], Surendiran Mohan[2*], A. Alvin Kalicharan[3], Sherlin Joseph[4], Shanmugam Anusuya[5], and Sudheshkannan Rajendran[6]

[1]Department of Chemistry, Vinayaka Mission's Kirupananda Variyar Arts and Science College, Vinayaka Mission's Research Foundation, Salem-636 308, India.

[2]Department of Humanities and Sciences-Chemistry, Centre for Nanotechnology Research, Aarupadai Veedu Institute of Technology, Vinayaka Mission's Research Foundation (DU), Paiyanoor, Chennai 603 104, India

[3]Department of Chemistry, Panimalar Engineering College (Autonomous), Poonamallee, Chennai - 600 123, India

[4]Centre for Advanced Functional Materials, Chennai Institute of Technology, Chennai-600069, Tamil Nadu, India.

[5]Department of Pharmaceutical Engineering, Vinayaka Mission's Kirupananda Variyar Engineering College, Vinayaka Mission's Research Foundation (Deemed to be University), Salem-636 308, India

[6]Scientist, Novitium Pharma LLC (ANI Pharmaceuticals), 70 Lake Drive, East Windsor, New Jersey 08520, USA

*Corresponding author E-mail: anbu80@gmail.com

Abstract

The unique characteristics of green synthesis have paved the way for innovative research on nanoparticle preparation within the scientific community. In the present study, an effective approach was employed to synthesize homogeneous and highly oriented Ag-doped ZnO nanoparticles using the extract of *Vinca rosea* (L.). The structural and morphological characteristics of the synthesised Ag–ZnO nanoparticles were examined using XRD, SEM, and TEM techniques. Antimicrobial activity was evaluated against various human-pathogenic bacteria, including *Staphylococcus aureus*, *Bacillus subtilis*, *Salmonella typhi*, and *Escherichia coli*, as well as the fungus *Aspergillus niger*. Cytotoxicity studies were carried out on breast (MCF-7) and lung (A549) cancer cell lines at different concentrations. In vitro antidiabetic activity was also assessed. Additionally, confocal laser scanning microscopy (CLSM) was used to evaluate dental biofilm inhibition. SEM analysis confirmed the flower-like morphology of the synthesized nanoparticles, while TEM images revealed continuous crystal planes, indicating high crystallinity. The Ag–ZnO nanoparticles exhibited significant antimicrobial activity against the tested microorganisms. The study also demonstrated notable anticancer effects, with dose-dependent increases in apoptosis in A549 and MCF-7 cells. Furthermore, the nanoparticles showed promising antidiabetic activity. CLSM analysis indicated that Ag–ZnO nanoparticles effectively reduced the viability of *Streptococcus mutans* biofilm on dentine in a time-dependent manner. The present work demonstrates a useful green synthesis approach

for developing Ag–ZnO nanostructures with multifunctional properties, including antimicrobial, anticancer, antidiabetic, and dental biofilm control activities, suggesting their potential application in biomedical fields.

Keywords: Green synthesis, *Vincarosea* (L), antidiabetic, cytotoxic effect, biofilm.

1. Introduction

The physicochemical approaches have been employed to synthesize nanoparticles in the past. However, they take a long time, require specific arrangements, and involve costly, toxic solvents or chemicals that may have harmful side effects [1]. The benefits of green nanoparticle synthesis are ease of use, low cost, environmental friendliness, and non-toxicity (NPs) [2]. Due to its novel characteristics, green synthesis has attracted the attention of numerous researchers worldwide. Because it produces the most stable nanoparticles in a variety of geometries, green metal nanoparticle synthesis is a desirable area of nanoscience [3]. Zinc oxide is an important inorganic pharmaceutical material due to its high activity, non-toxicity, ability to generate reactive oxygen species (ROS), and essential role in human metabolism [4]. The ZnO nanoparticles are environmentally friendly, non-toxic, biosafe, and biocompatible. [5]. Due to their biological applications, ZnO nanoparticles are useful for gene therapy, wound healing, biological sensing, drug delivery, agriculture, food additives, and antibacterial activity [6].

Additionally, ZnO NPs were discovered to have a greater influence on rheological parameters [7]. They are also reasonably priced and diverse in terms of morphology, including nanotubes, nanoflowers, nanorods, and nanospheres. Metal oxide nanoparticles have been widely exploited as functional materials in a variety of applications. Due to their broad spectrum of anticancer, antidiabetic, and antibacterial activities, metal oxide nanoparticles such as FeO [8], ZnO [9], CeO_2 [10], and Ag [11] have attracted considerable attention. Since Ag is comparatively less toxic and has excellent oxygen-adsorption properties, surfaces coated with Ag are significantly more effective at preventing pathogen infections [12]. Ag-ZnO NPs have received extensive research attention due to their superior antibacterial and antifungal activity for biomedical applications such as drug delivery, cancer treatment, dye degradation, dye absorption, and more [13]. The therapeutic benefits of *Vinca rosea* have been widely established and supported by the experience of traditional Ayurvedic practitioners [14]. *Vincarosea* extracts have been shown to inhibit hepatic carcinogen-metabolizing enzymes and to exhibit potential anticancer activity [15]. The similar properties and characteristics of metal-doped materials, such as K-ZnO [16], SiO2-ZnO [17], and Ag-ZnO [18], etc., are more attractive to scientists. Due to their exceptional universal features and enhanced properties compared with monometallic nanoparticles, they have attracted considerable attention recently. In this regard, composites containing monometallic NPs and doped metal oxides are more appealing and have great potential for biomedical applications. ZnO NPs have gained significant attention due to their functional properties. Ag–ZnO can be prepared by doping ZnO NPs with Ag, thereby enhancing their anticancer and antibacterial activities, as the interaction between ZnO and Ag in Ag–ZnO NPs effectively suppresses bacterial growth. Compared with physicochemical and biological processes, green synthesis has emerged as a viable option for NP synthesis. Since green-synthesized nanoparticles conjugated with Vinca alkaloids are associated with higher particle stability, they are biodegradable, homogeneous in shape, stable, and less toxic. They have increased the biomedical activities of metallic NPs. Green synthesis of Ag-ZnO NPs has been reported from various plants, such as *Verbascum speciosum* [19], *Morinda citrifolia* [20], *Beta vulgaris* [21], *Pseudovernia furfuracea* [22],

and *Morus macroura* [23]. Phytochemical investigations of *Vincarosea* have been published, and its extract has been found to have antidiabetic, antiviral, antimicrobial, and anticancer properties [24]. It is also the main component of anticancer alkaloids like vincristine and vinblastine, and antidiabetic alkaloids like vindoline (Fig. 1). In this study, we report the morphology, antidiabetic, antimicrobial, and anticancer properties of Ag-ZnO NPs prepared using *Vincarosea (L).* The development of Ag-ZnO NPs using medicinal agents has emerged as an exciting field of study. It inspired us to use a green way to make Ag-ZnO nanostructures. Because *Vincarosea (L),* the main reducing agent, is one of the best-known medicinal plants on Earth, the process is environmentally beneficial. As a reducing agent, *Vincarosea (L)* reduces the need for additional synthetic reducing agents.

2. Methods

Zinc acetate and silver nitrate were purchased from Sigma-Aldrich and used as such without further purification. The bacterial cultures of *S. aureus, B. subtilis (Gram-positive), S. typhi, E. coli (Gram-negative), and A. niger (Fungi) were purchased from the* MTCC culture center, Chandigarh, India.

2.1 *Vincarosea (L)* collection and extract preparation

Vincarosea (L) plants were collected from the Dharmapuri district of Tamil Nadu. *Vincarosea* green leaves are properly cleaned in distilled water, allowed to dry at room temperature, and then ground into a fine powder. 10 gm of *Vincarosea* plant leaves powder was boiled in 100 mL of distilled water for 30 minutes at 60°C. The resulting brown-colored solution was filtered through Whatman No. 1 filter paper and then stored in the freezer for further processing.

2.2 Preparation of Ag-doped ZnO NPs

Ag-ZnO NPs were prepared using a green combustion technique with a slight modification. Zinc acetate and silver nitrate were used as the precursors. A 0.5 M zinc acetate solution was prepared in 100 mL of water. Then, 40 mL of *Vincarosea (L)* extract and 0.5 M $AgNO_3$ were added to the zinc acetate solution over 2 hours with constant stirring. The black precipitate was filtered using Whatman No. 1 filter paper and then calcined at 450 °C for 3 hours. The green synthetic process of Ag-ZnO NPs is shown in **Fig.** 1.

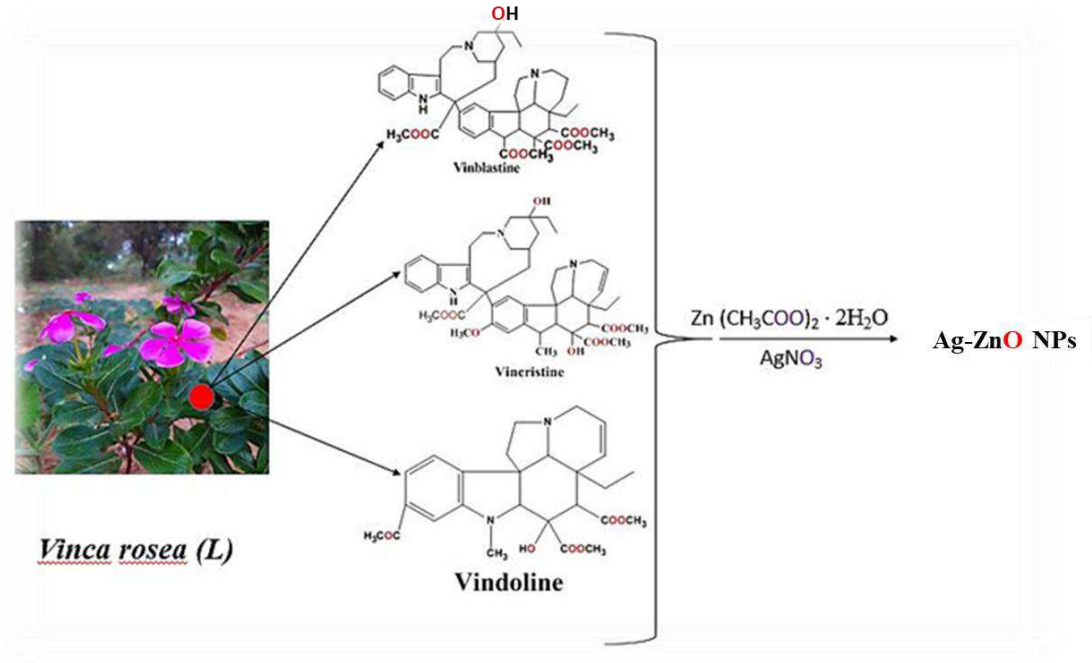


Fig. 1. Schematic diagram of the synthesis of Ag-ZnO NPs

2.3 Characterization

2.3.1 Structure and Morphology

The XRD patterns of the Ag-ZnO NPs were examined using SHIMADZU XRD 6000. SEM and TEM were used to analyze the three-dimensional structure. EDX analysis was performed utilizing an INCA PENTA FET X3 system attached to the SEM (JSM 6390). UV–Vis absorption spectra were recorded using a JASCO-V-750 spectrophotometer with a wavelength range of 300-800 nm. The functional group of Ag-ZnO NPs was analyzed using FTIR IR Affinity in the range of 460-4000 cm^{-1}.

2.3.2 Cytotoxicity effect

MTT (3-(4,5-dimethylthiazol-2-yl)-2,5-diphenyltetrazolium bromide) was used to assess the sample's cytotoxicity against MCF7 and A549 cell lines. The cells were seeded in 96-well microplates and cultured in an incubator at 37 °C for 48 hours, allowing them to achieve 70-80% confluence. The medium was replenished, and the cells were cultured for 24 hours at various concentrations (20, 40, 60, 80, and 100 µg/mL) [25]. After 24 hours, the morphological changes of treated and untreated cells were evaluated and photographed using a digital inverted microscope. The cells were then rinsed in phosphate buffer saline (PBS, pH 7.4), and 20 mL of MTT solution and 5 mg/mL of nanomaterial in PBS were added to each well. Afterward, the plates were kept at 37 °C in the dark for 2 hours. After the formazan substance had been dissolved in 100 mL of DMSO, the absorbance maximum at 570 nm was measured by recording a UV spectrum. Cell viability percentage was calculated using the following formula. Where A_S is the absorbance of the sample, and A_C is the absorbance of the control of the sample.

$$\text{Cell viability (\%)} = \left(\frac{As}{Ac}\right) 100$$

2.3.3 Antidiabetic activity

The 3,5-dinitrosalicylic acid (DNSA) reagent was used to detect reducing sugars using the α-amylase activity method. 500 µg/mL of phosphate buffer was mixed (0.02 M phosphorus buffer, pH 6.9, including 0.005 M NaCl, 10 µL of α-amylase solution (10 mg/mL) with various concentrations (50 to 250 µg/mL), and then 500 µg/ mL of starch solvent (1%) in the tube. After 15 minutes of incubation at 25 °C, the mixture was incubated again in the tube for 1 hour. 0.5 mL of DNSA was added, and the mixture was then immersed in cold water for 10 min. At 540 nm, the sample's intensity was measured. The absorbance at 540 nm was measured to determine the activities of the sample, substrates, and blank amylase under the same conditions. Enzyme inhibition activity was calculated using the following formula. Where *Ac* and *As* are the absorbance of the standard and Ag-ZnO NPs sample.

$$\text{Inhibition (\%)} = (Ac - As)\left(\frac{100}{Ac}\right)$$

2.3.4 Antimicrobial activity

3.8 g/100 mL of Muller-Hinton agar (MHA) and 3.5 g/100 mL of potato dextrose agar (PDA) medium were prepared in separate flasks and autoclaved at 121 °C [26]. The medium was poured into a Petri dish after sterilization and incubated at 37 °C for 1 hour. The plates were inoculated with the microbial strains, the test samples (25 to 100 µg/mL) were loaded into the respective wells, and the plates were incubated at 37 °C overnight. After incubation, the zone of inhibition was measured and recorded.

3. Results

3.1 X-Ray Diffraction

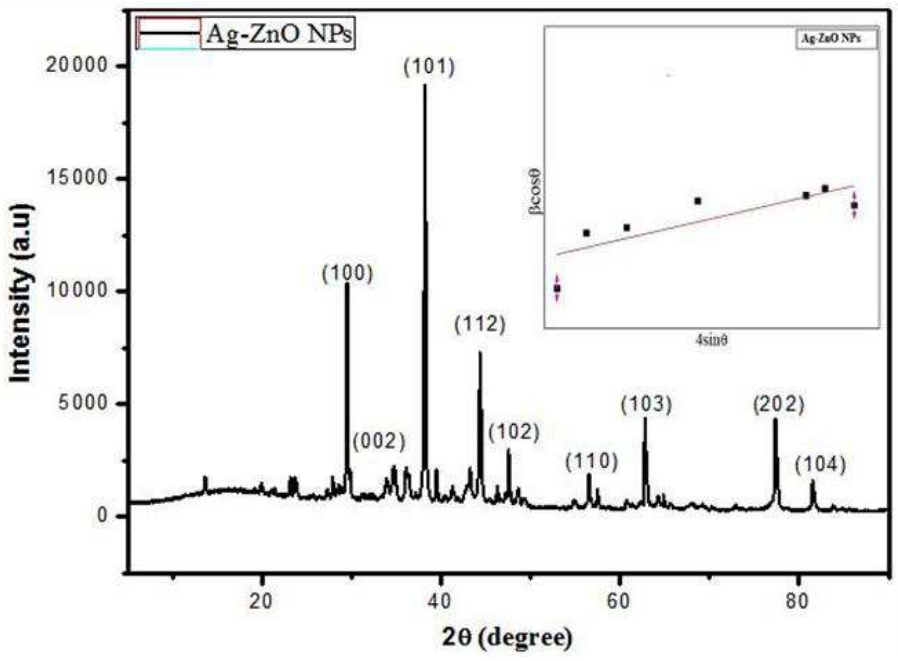


Fig. 2 XRD pattern of Ag-ZnO NPs

The XRD pattern of Ag-ZnO NPs prepared with *Vincarosea (L)* is shown in **Fig. 2**. The XRD patterns exhibit diffraction peaks at 28.80º, 39.12º, 42.5º, and 63.6º, which correspond to the (100), (101), (112), and (103) planes of ZnO hexagonal structure [JCPDS file 89-1397]. No additional phase was seen in the XRD pattern. The lattice strain and crystallite size of Ag-ZnO NPs were calculated using the Scherrer formula and the Williamson-Hall equation, shown below equations (1) and (2), respectively [27].

$$D = \frac{0.89\lambda}{\beta cos\theta} \quad (1)$$

$$\beta hkl\cos\theta = \frac{0.89\lambda}{D} + 4\eta\sin\theta \quad (2)$$

where: *D* is the crystallite size, λ is the wavelength, K is the Scherrer constant, and θ is the Bragg angle. The lattice constant and crystallinity index (CI) of the prepared hexagonal Ag-ZnO NPs were calculated using the following equations (3) and (4), respectively. The calculated average crystallite size, lattice strain, lattice constants, and crystallinity index (CI) were tabulated in **Table 1.**

$$n\lambda = 2d\sin\theta \quad (3)$$

$$\frac{1}{d^2} = \frac{4}{3}\left(\frac{(h^2+k^2+hk)}{a^2}\right) + \frac{l^2}{c^2} \quad (4)$$

where *n* is the order of diffraction, and *d* is the spacing between planes (*h*, *k*, and *l*) of given Miller indices. The c/a ratio was determined to be around 1.60, which is extremely close to the usual value of 1.60 for the hexagonal structure.

Table: 1. Ag-ZnO NPs Lattice parameters

Crystallite size D (nm)		**Crystallinity index (CI) (%)**	**Lattice parameters (Å)**		**Lattice strain Ɛ (*10^{-4})**
Williamson-Hall	Scherrer		a=b	c	
43	39	1.34	3.19	5.12	6.06

3.2. FTIR Spectrum

The bending and stretching vibrations of the synthesized material are investigated using FT-IR. As shown in **Fig. 3**, Ag-ZnO NPs exhibit distinctive vibrational modes. The Ag-ZnO NP linkages are represented by the peaks that range from 500 to 1000 cm^{-1} [28]. The appearance of a peak at approximately 709 cm^{-1} could be caused by Ag-ZnO. The strong peak at 1420 cm^{-1} is due to the presence of >C=C<. The peaks at 1797 and 2511 cm^{-1} could be due to a small amount of moisture in the sample. O-H bending vibrations are weakly present, as shown by a slight peak at around 1797 cm^{-1}.

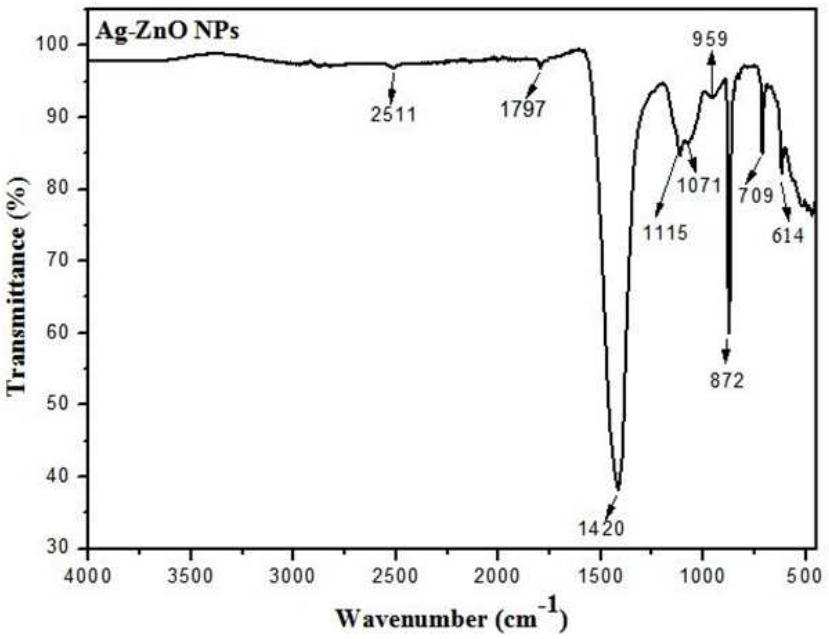


Fig. 3 FT-IR spectrum of Ag-ZnO NPs

3.3. SEM and TEM study

The surface morphology of Ag-ZnO NPs and the particle size histogram are shown in **Fig. 4(A-D)**. SEM image revealed the flower-like structure, as shown in **Fig. 4(A)** [29]. The crystal formation and larger particles observed in these products could be due to the Ag doping. In green synthesis, plant extracts were used as the solvent medium and acted as binding agents between particles, facilitating the self-assembly process that produces nanocrystals. In general, organic additives interspace the nanostructures in a microscale transformation, although even in the absence of additives, alignment order and faceted microstructures can occur. **Fig. 4(B)** depicts a TEM image of the sample that exhibits the agglomeration of the particles. This TEM image shows the sample from the side and supports the SEM observation that small thin films are forming a flowerlike structure. The continuous pattern of all planes, as shown in the SEAD pattern, is shown in **Fig. 4(C)**. The average particle size histogram is given in **Fig. 4D** (average particle size 6.1 nm). The crystalline nature of the prepared nanoparticles is revealed in **Fig. 4(C).**

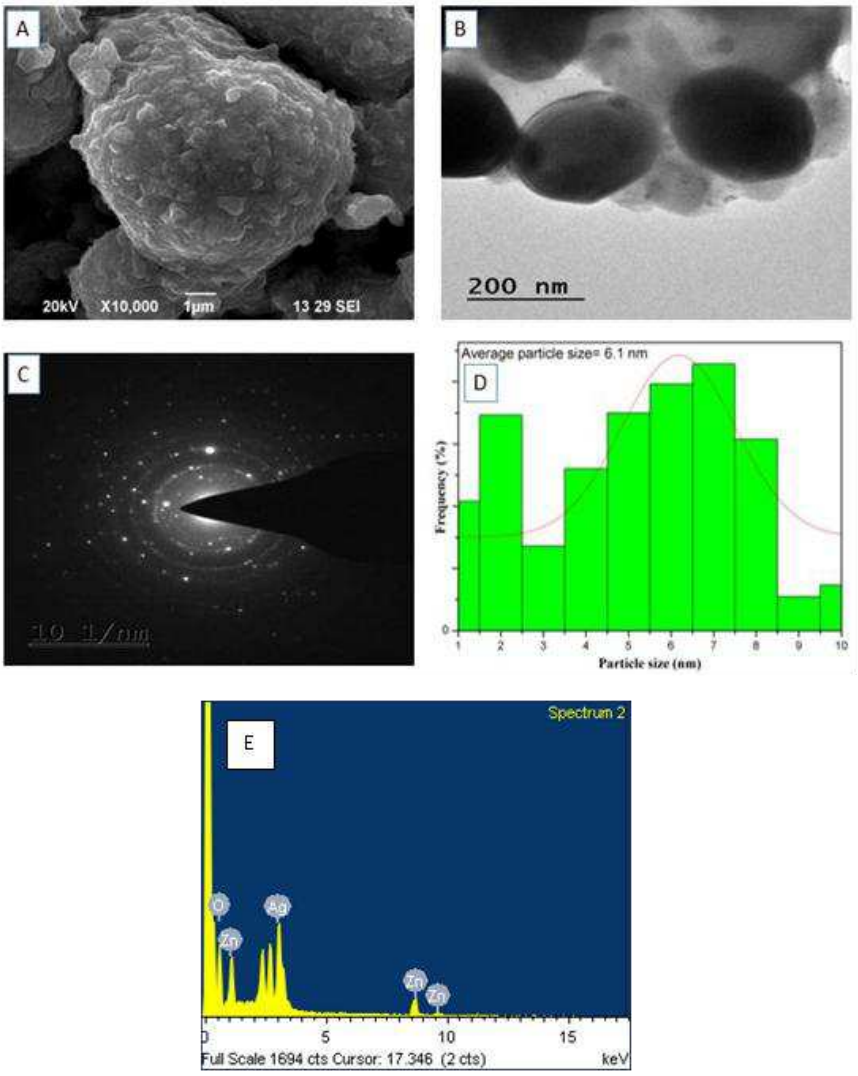


Fig. 4(A) SEM image of Ag-ZnO NPs, (B) TEM image of Ag-ZnO NPs, (C) SEAD of Ag-ZnO NPs, (D) Histogram diagram of Ag-ZnO NPs, and (E) EDX pattern of Ag-ZnO NPs.

Table 2. Elemental composition of Ag-ZnO NPs

S. No	Element	Weight %	Atomic %
1	O	45.29	82.21
2	Zn	17.50	7.77
3	Ag	37.21	10.02

Fig 4(E) shows the EDX pattern of Ag-ZnO NPs and provides the elemental percentage analysis. The peaks of zinc, silver, and oxygen associated with feces, which together can function as silver-doped ZnO NPs. Zinc and silver are the predominant elements, making up more than half of the total composition, along with oxygen, suggesting that Ag-ZnO NPs have formed [30]. This shows that a green synthesis method can be used to

produce nanoparticles easily. The atomic and weight percentages of the elements present in the nanoparticle are given in the **table. 2**.

3.4 UV–Vis Spectroscopy

UV–Vis absorption spectrum of Ag-ZnO NPs is shown in **Fig.5**. The strong absorption peak at 415 nm indicates that Ag is coated on the surface of ZnO NPs. The fluctuation in the absorption peak edges is due to the embedding of ZnO NPs by Ag NPs, which results in an electron crossing from the valence band to the conduction band. Ag-ZnO NPs exhibit a strong peak in the UV region, indicating that the particles are highly doped and nanoscale. The Tauc's relation was used to determine the bandgap energy of Ag-ZnO NPs,

$$(\alpha h\nu)1/2 = A(h\nu - Eg)$$

Where h is the Planck constant, ν is the photon's frequency, Eg is the band gap energy, and A is a constant. This relationship was derived by deducing the linear section of the $(\alpha h\nu)^{1/2}$ eV vs energy (eV) plot. The Tauc plot of the absorption spectra of Ag-ZnO NPs for deducing the bandgap energies is shown in the inset of **Fig. 5**, and the calculated value is 3.3 eV [31-33].

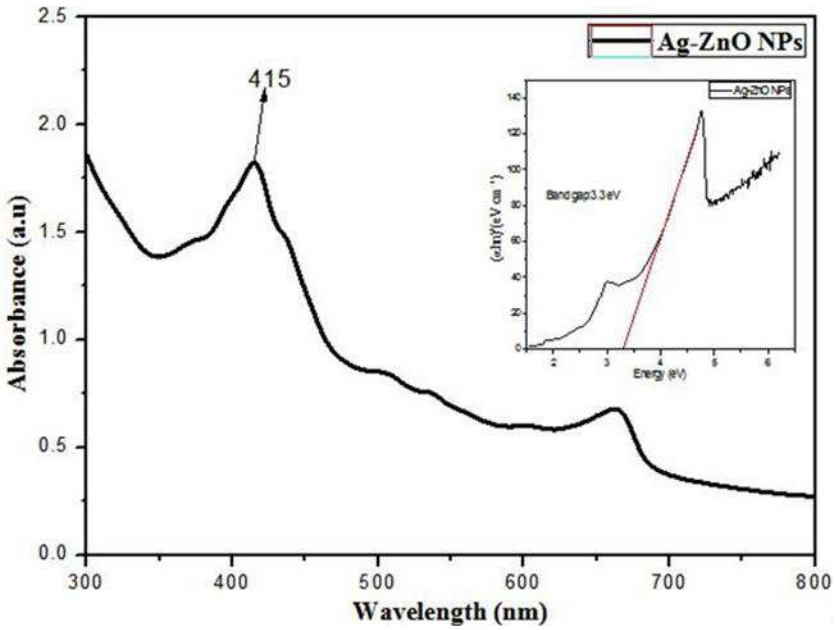


Fig. 5. UV spectrum of Ag-ZnO NPs

3.5 Cytotoxic effects

The cytotoxic effects of Ag-ZnO NPs at five concentrations (20-100 g/mL) were examined in the study using the human cell lines A549 and MCF7 [34]. The Ag-ZnO NPs reduced cell viability after 24 hours of treatment. Lesser concentrations (20 g/mL) of Ag-ZnO NPs are highly harmful to A549 cell lines, like how higher concentrations of Ag-ZnO NPs (100 g/mL) are significantly more dangerous to MCF7 than their comparable A549 cell line. These differences in the cytotoxicity of Ag-ZnO NPs (**Fig. 6**) may be due to interactions with proteins, the generation of ROS, or their ability to activate intrinsic apoptotic mechanisms. Smaller NPs can enter

cells and organelles more readily, increasing their likelihood of causing oxidative stress and death. The cytotoxicity of Ag-ZnO NPs against MCF7 cells at higher concentrations was more affected by their green production. [35-36]. At lower doses, Ag-ZnO NPs exhibited a somewhat stronger cytotoxic effect on A549 cells, but these differences were not statistically significant. In addition, in contrast to previous reports, we found that the size and surface of the Ag-ZnO NPs affected their ability to kill A549 and MCF7 cells.

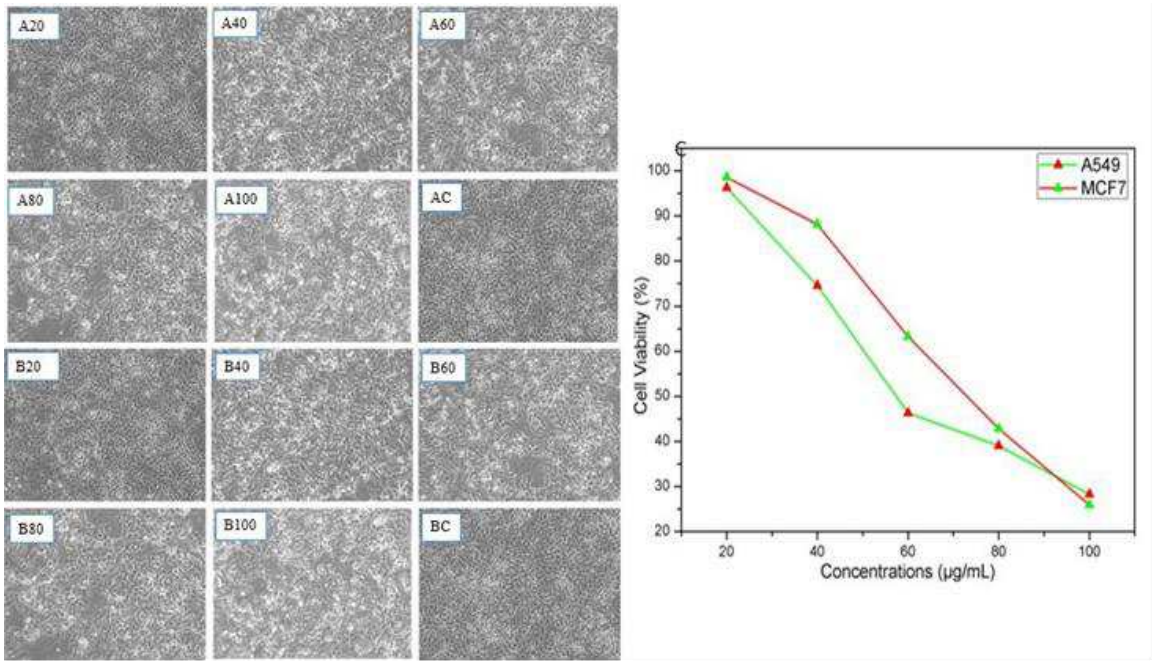


Fig. 6. Cytotoxicity effect of Ag-ZnO NPs

3.6 Biological Activity Studies

3.6.1 Antidiabetic Activity (α-amylase)

The Ag-ZnO NPs have been observed to inhibit α-amylase. The Ag-ZnO NPs exhibited the maximum inhibition efficiency during the study. Inhibition increased with successive nanoparticle doses, as indicated by the concentration-percentage inhibition plot. The greatest performance of the Ag-ZnO NPs begins at a concentration of 250 µg/mL (88.37 %). Therefore, Ag-ZnO NPs derived from the α-amylase enzyme are selective-action inhibitors (IC_{50}: 74.1 µg/mL). Ag-ZnO NP efficiency decreases to 85% at a dosage of 250 µg/mL (Fig. **7A**).

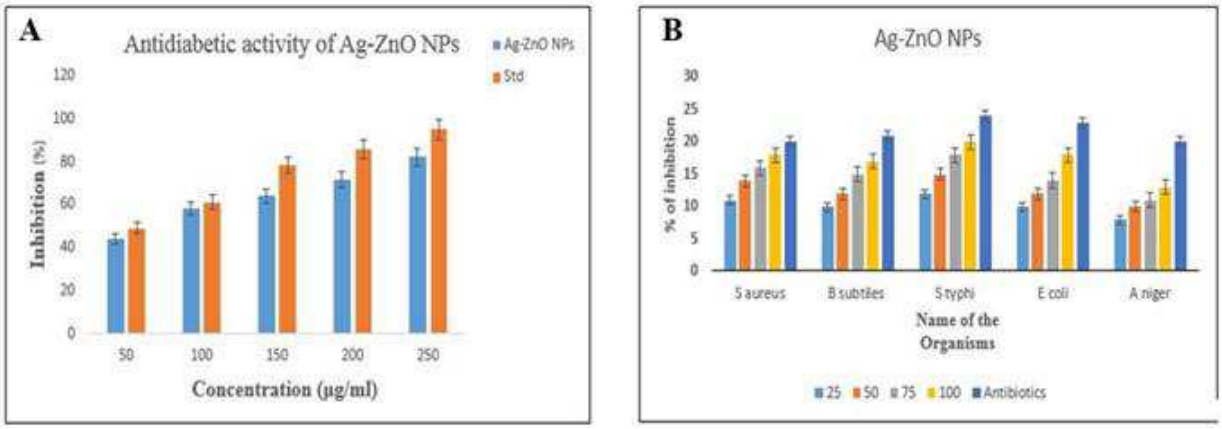


Fig. 7 A. Antidiabetic & B. Antimicrobial activity of Ag-ZnO NPs

3.6.2 Antimicrobial activity

The antimicrobial activity and inhibitory zones (in mm) of Ag-ZnO against Gram-negative and Gram-positive bacteria, as well as its antifungal activity, were studied and presented in **Fig. 7B**. The inhibition zones were measured in mm units using the Ag-ZnO nanoparticles solution. As shown in **Fig. 7B**, antimicrobial activity against *S. typhi* and *S. aureus* is significantly higher than that against other organisms. As observed across all organisms examined, the Ag-ZnO NPs exhibited the largest inhibitory zone against *S. typhi* (20 mm at 100 µg/mL). *aureus* (18 mm), and the lowest inhibitory zone against *A. niger* (13 mm in 100 µg/mL).

3.7 CLSM images of *Streptococcus mutans* biofilms on dentine surfaces after LCD treatment

Confocal laser scanning microscopy (CLSM) images of *Streptococcus mutans* biofilms on dentine surfaces treated with LCD. Three-dimensional confocal laser scanning microscopy (CLSM) images of live/dead staining of *S. mutans* biofilms growing on dentine surfaces after different treatments. Acridine orange (green) stains live cells, and propidium iodide (red) stains dead or damaged cells. **Fig. 8(a-d)** are surface views, and (e-h) are views of the deeper layers of the biofilms. (a, e) Control group (no LCD) with strong green fluorescence, showing a rich and highly viable biofilm with few dead cells. **Fig. 8(b, f)** 12 h LCD-treated biofilms showing decreased green fluorescence and a significant increase in red fluorescence, suggesting a reduction in cell viability and membrane damage. **Fig. 8(c, g)** 24 h LCD-treated biofilms showing further reduction in green fluorescence and enhanced red fluorescence, indicating continued antibacterial effect and a decrease in biofilm viability. **Fig. 8(d, h)** Overlay and depth-coded images showing the distribution of live and dead cells at different depths of the biofilm, with increasing red fluorescence over time.

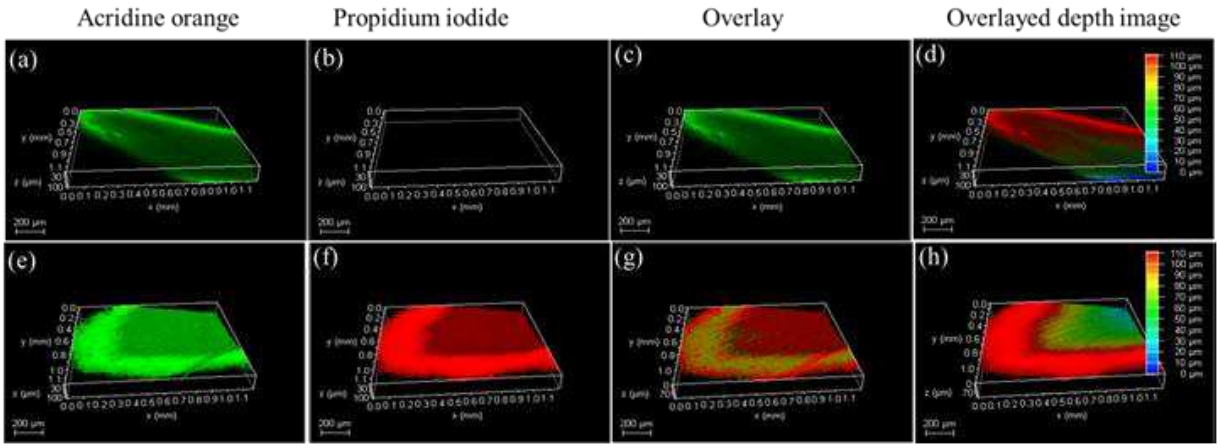


Fig. 8. Confocal laser scanning microscopy (CLSM) images of Streptococcus mutans biofilms grown on dentine surfaces treated with LCDs. (a, e) Control group with a high proportion of live cells (green fluorescence). (b, f) Biofilms exposed to 100 µg/mL LCDs for 12 h showed diminished green and enhanced red fluorescence, suggesting a reduction in the number of live cells. (c, g) Biofilms treated with LCDs for 24 h showed fewer live cells and more dead cells. (d, h) Overlay and coded images showing the location of live and dead cells in the biofilm.

4. Discussion

The results are discussed with respect to their structural significance and potential applications. The significant broadening of the observed diffraction peaks indicates the formation of nanoscale crystallites. The increased peak broadening is mainly due to a smaller crystallite size and lattice micro strain. Low internal stress indicates the formation of a stable nanophase. Further insights were gained from the Williamson-Hall (W-H) analysis, which suggested that the line broadening is predominantly isotropic. The linear fit to the W-H plot yields a positive slope and a nonzero intercept, confirming the combined effect of crystallite size and lattice strain on peak broadening. These results clearly suggest that the size- and strain-induced effects are important in determining the structural properties of the synthesized nanoparticles.

The peaks in the range of 500–1000 cm^{-1} are attributed to Ag–ZnO NP linkages. The peak around 709 cm^{-1} may be assigned to the Ag-ZnO interaction. The strong peak at 1420 cm^{-1} is due to >C=C< stretching vibrations. The peaks at 1797 cm^{-1} and 2511 cm^{-1} can be attributed to a small amount of moisture in the sample. The weak O–H bending vibration at around 1797 cm^{-1} also indicates the presence of moisture. The FT-IR study revealed that all peaks are attributed to the green-synthesized Ag–ZnO NPs.

The crystallization and the presence of larger particles in these products may be due to the Ag dopant. In green synthesis, plant extracts were used as the solvent medium and also served as binding agents between particles, facilitating self-assembly and nanocrystal formation. In general, the organic additives function to interspace the nanostructures during a microscale transformation. However, even without the help of additives, the order of alignment and faceted microstructures can occur. The most abundant elements are zinc and silver, which together account for more than half of the total components and, in combination with oxygen, indicate the formation of Ag-ZnO NPs [30]. The energy of the bandgap in Ag-ZnO NPs is attributed to Ag particles being

incorporated into the ZnO NPs [31]. The reduction in bandgap value as compared to the reported values of ZnO nanoparticles, particularly in the dopant, could be due to a variety of factors, including the higher energy of electrons resulting in an electron transfer from the conduction band of Ag to the ZnO encapsulated material, lattice structure, and the change in ionic radii of Ag and Zn ions [32-33]. The variations in cytotoxicity of Ag-ZnO NPs may be due to protein interactions, ROS production, or their ability to induce intrinsic apoptotic mechanisms. Smaller NPs can more easily enter cells and organelles, thereby increasing their ability to induce oxidative stress and death. The cytotoxicity of Ag-ZnO NPs towards MCF7 cells was more affected by the green production of these NPs at higher concentrations [35-36]. Moreover, we found that the size and surface of the Ag-ZnO NPs affected their ability to kill A549 and MCF7 cells, which is contrary to the previous reports.

At higher doses, the inhibition of α-amylase activity by nanoparticles increases, with reduced selectivity. Based on current results, it is evident that green-synthesized Ag-ZnO NPs are more inhibitory, depending on nanoparticle size and on the coating (e.g., vindolicine and vindollidine, alkaloids). The inhibition zone results indicate that the mechanism of Ag-ZnO NPs' activity involves membrane disruption coupled with rapid growth of surface oxygen species, ultimately leading to pathogen mortality. Surprisingly, the size of the inhibitory zone varied with the pathogens, manufacturing process, and nanoparticle concentration. Bactericidal was defined as the absence of growth around the bacteria's inhibitory zones. Several researchers discovered that *Vincarosea (L)* has antibacterial activity against several diseases. At a concentration of 200 µg/mL, ZnO nanoparticles from *Vincarosea* leaves exhibit antimicrobial activity against Gram-positive and Gram-negative bacteria. *Vincarosea* leaf extract had poor activity against *S. aureus* (18 mm) [33], and Mn-doped Cu nanoparticles had minimum activity against *E. coli* (16.3 mm). The results demonstrate that green-synthesized Ag-ZnO NPs have outstanding antimicrobial activity.

The CLSM results demonstrated that LCD treatment significantly reduced the viability of Streptococcus mutans biofilms, as evidenced by decreased green fluorescence and increased red fluorescence. The effect is time-dependent and more pronounced at 24 h than at 12 h. The depth-wise distribution of red fluorescence suggests that the treatment penetrates the biofilm and damages cells along the structure. Overall, LCD significantly disrupted biofilm integrity and viability.

5. Conclusion

In this study, highly oriented and uniform Ag-ZnO NPs were synthesized using an eco-friendly method through a systematic process employing *Vinca rosea* (L.*)* extract. Alkaloids from *Vinca rosea (L)* have been used to reduce metal salts to make nanostructures. The XRD pattern of the Ag-ZnO NPs reveals their crystalline phases. The nanoparticle size was determined using the Williamson-Hall and Scherrer techniques to be approximately 43 nm and 39 nm, respectively. The sample's flower-like structure was observed using SEM. The TEM studies reveal the crystal's continuous plane, and the SEAD pattern confirms the sample's excellent crystallinity. According to FTIR analysis, the functional groups in *Vincarosea* alkaloids stabilized the Ag-ZnO NPs. The antimicrobial properties of the Ag-ZnO NPs produced were found to inhibit the growth of various pathogenic bacteria (Gram-positive and Gram-negative). Notably, the nanoparticles were discovered to have antifungal qualities against fungus strains (*A. niger*). As a result, these nanostructures could be employed to fight diseases as preventive or chemotherapeutic agents. Green synthesis is more effective at producing stable, safer nanoparticles than chemical-

based approaches, which are less stable and less environmentally benign. The environmentally friendly Ag-ZnO nanoparticles investigated, prepared from *Vinca rosea (L.)* extract, are anticipated to have a wide range of applications in the formulation of antimicrobial, antidiabetic, and cytotoxic products across agriculture, medicine, and the pharmaceutical industry.

DECLARATIONS

Ethical approval: This study does not involve human participation or animal testing. Hence, ethical approval is not required.
Funding: No funding was received for conducting this study.

Reference

[1] B. D. Deshpande, P. S. Agrawal, M. K. N. Yenkie, and S. J. Dhoble, "Prospective of nanotechnology in degradation of waste water: A new challenges", *Nano-Struct. Nano-Objects*, vol. 22, p. 100442, 2020, doi: https://doi.org/10.1016/j.nanoso.2020.100442.

[2] Swati, Ritesh Verma, Ankush Chauhan, Mamta Shandilya, Xiangkai Li, Rajesh Kumar, Saurabh Kulshrestha, "Antimicrobial potential of ag-doped ZnO nanostructure synthesised by the green method using moringa oleifera extract," *J. Environ. Chem. Eng.*, vol. 8, no. 3, p. 103730, 2020, doi: https://doi.org/10.1016/j.jece.2020.103730.

[3] Kisimba, K., Krishnan, A., Faya, M., Byanga, K., Kasumbwe, K., Vijayakumar, K., & Prasad, R. (2023). Synthesis of metallic nanoparticles based on green chemistry and their medical biochemical applications: synthesis of metallic nanoparticles. *Journal of Renewable Materials*, *11*(6), 2575-2591.https://doi.org/10.32604/jrm.2023.026159

[4] H. Mirzaei and M. Darroudi, "Zinc oxide nanoparticles: Biological synthesis and biomedical applications," *Ceram. Int.*, vol. 43, no. 1, Part B, pp. 907–914, 2017, doi: https://doi.org/10.1016/j.ceramint.2016.10.051.

[5] Ramya, V.; Kalaiselvi, V.; Kannan, S. Karthik; Shkir, Mohd.; Ghramh, Hamed A.; Ahmad, Zubair; Nithiya, P.; Vidhya, N, "Facile Synthesis and Characterization of Zinc Oxide Nanoparticles Using Psidium guajava leaf Extract and Their Antibacterial Applications," *Arab. J. Sci. Eng.*, vol. 47, no. 1, pp. 909–918, 2022, doi: 10.1007/s13369-021-05717-1.

[6] M. Azmana, S. Mahmood, A. R. Hilles, A. Rahman, M. A. Bin Arifin, and S. Ahmed, "A review on chitosan and chitosan-based bionanocomposites: Promising material for combatting global issues and its applications," *Int. J. Biol. Macromol.*, vol. 185, pp. 832–848, 2021, doi: https://doi.org/10.1016/j.ijbiomac.2021.07.023.

[7] S. Thakur, S. Neogi, and A. K. Ray, "Morphology-controlled synthesis of ZnO nanostructures for caffeine degradation and escherichia coli inactivation in water," *Catalysts*, vol. 11, no. 1, pp. 1–18, 2021, doi:

10.3390/catal11010063.

[8] P. Karpagavinayagam and C. Vedhi, “Green synthesis of iron oxide nanoparticles using Avicennia marina flower extract,” *Vacuum*, vol. 160, pp. 286–292, 2019, doi: https://doi.org/10.1016/j.vacuum.2018.11.043.

[9] J. Xu, Y. Huang, S. Zhu, N. Abbes, X. Jing, and L. Zhang, “A review of the green synthesis of ZnO nanoparticles using plant extracts and their prospects for application in antibacterial textiles,” *J. Eng. Fiber. Fabr.*, vol. 16, 2021, doi: 10.1177/15589250211046242.

[10] A. Miri, H. Beiki, A. Najafidoust, M. Khatami, and M. Sarani, “Cerium oxide nanoparticles: green synthesis using Banana peel, cytotoxic effect, UV protection and their photocatalytic activity,” *Bioprocess Biosyst. Eng.*, vol. 44, no. 9, pp. 1891–1899, 2021, doi: 10.1007/s00449-021-02569-9.

[11] G. A. Naikoo *et al.*, “Bioinspired and green synthesis of nanoparticles from plant extracts with antiviral and antimicrobial properties: A critical review,” *J. Saudi Chem. Soc.*, vol. 25, no. 9, p. 101304, 2021, doi: https://doi.org/10.1016/j.jscs.2021.101304.

[12] M. M. Said *et al.*, “Multifunctional hydroxyapatite/silver nanoparticles/cotton gauze for antimicrobial and biomedical applications,” *Nanomaterials*, vol. 11, no. 2, pp. 1–25, 2021, doi: 10.3390/nano11020429.

[13] M. Ehsan *et al.*, “Plant-Based Bimetallic Silver-Zinc Oxide Nanoparticles: A Comprehensive Perspective of Synthesis, Biomedical Applications, and Future Trends,” *Biomed Res. Int.*, vol. 2022, p. 1215183, 2022, doi: 10.1155/2022/1215183.

[14] S. Martinotti and E. Ranzato, “3 - Natural compounds and anticancer effects: The whole is greater than the sum of its parts,” Y. B. T.-F. F. in C. P. and T. Kabir, Ed. Academic Press, 2020, pp. 47–58. doi: https://doi.org/10.1016/B978-0-12-816151-7.00003-X.

[15] Y. Elhassaneen, S. Ragab, A. Abd El-Rahman, and S. Arafa, “Vinca (Catharanthus roseus) Extracts Attenuate Alloxan-Induced Hyperglycemia and Oxidative Stress in Rats,” *Am. J. Food Sci. Technol.*, vol. 9, no. 4, pp. 161–172, 2021, doi: 10.12691/ajfst-9-4-8.

[16] M. Haghighat *et al.*, "Cytotoxicity properties of plant-mediated synthesised K-doped ZnO nanostructures," *Bioprocess Biosyst. Eng.*, vol. 45, no. 1, pp. 97–105, 2022, doi: 10.1007/s00449-021-02643-2.

[17] D. S. Bharathi, A. Boopathyraja, S. Nachimuthu, and K. Kannan, "Green Synthesis, Characterisation and Antibacterial Activity of SiO2–ZnO Nanocomposite by Dictyota bartayresiana Extract and Its Cytotoxic Effect on HT29 Cell Line," *J. Clust. Sci.*, 2021, doi: 10.1007/s10876-021-02170-w.

[18] B. Ranjithkumar *et al.*, “Evaluation of structural, surface morphological and thermal properties of Ag-doped ZnO nanoparticles for antimicrobial activities,” *Phys. E Low-dimensional Syst. Nanostructures*, vol. 133, p. 114801, 2021, doi: https://doi.org/10.1016/j.physe.2021.114801.

[19] S. M. Mousavi-Kouhi, A. Beyk-Khormizi, M. S. Amiri, M. Mashreghi, and M. E. Taghavizadeh Yazdi, “Silver-zinc oxide nanocomposite: From synthesis to antimicrobial and anticancer properties,” *Ceram. Int.*, vol. 47, no. 15, pp. 21490–21497, 2021, doi: https://doi.org/10.1016/j.ceramint.2021.04.160.

[20] K. Shreema, R. Mathammal, V. Kalaiselvi, S. Vijayakumar, K. Selvakumar, and K. Senthil, “Green synthesis of silver doped zinc oxide nanoparticles using fresh leaf extract Morinda citrifoliaand its antioxidant potential,” *Mater. Today Proc.*, vol. 47, pp. 2126–2131, 2021, doi: https://doi.org/10.1016/j.matpr.2021.04.627.

[21] P. C. Nagajyothi, P. Muthuraman, C. O. Tettey, K. Yoo, and J. Shim, "In vitro anticancer activity of eco-friendly synthesised ZnO/Ag nanocomposites," *Ceram. Int.*, vol. 47, no. 24, pp. 34940–34948, 2021, doi: https://doi.org/10.1016/j.ceramint.2021.09.035.

[22] F. D. Koca, M. G. Halici, Y. Işik, and G. Ünal, “Green synthesis of Ag-ZnO nanocomposites by using Usnea florida and Pseudevernia furfuracea lichen extracts and evaluation of their neurotoxic effects,” *Inorg. Nano-Metal Chem.*, pp. 1–8, May 2022, doi: 10.1080/24701556.2022.2078351.

[23] S. Anjum *et al.*, “Light tailoring: Impact of UV-C irradiation on biosynthesis, physiognomies, and clinical activities of Morus Macroura-mediated monometallic (Ag and ZnO) and bimetallic (Ag and ZnO) nanoparticles,” *Int. J. Mol. Sci.*, vol. 22, no. 20, 2021, doi: 10.3390/ijms222011294.

[24] S. Chandrasekaran, S. Anusuya, and V. Anbazhagan, “Anticancer, Anti-diabetic, Antimicrobial Activity of Zinc Oxide Nanoparticles: A Comparative Analysis,” *J. Mol. Struct.*, p. 133139, 2022, doi: https://doi.org/10.1016/j.molstruc.2022.133139.

[25] A. Hussain *et al.*, “Biogenesis of ZnO nanoparticles using: Pandanus odorifer leaf extract: Anticancer and antimicrobial activities,” *RSC Adv.*, vol. 9, no. 27, pp. 15357–15369, 2019, doi: 10.1039/c9ra01659g.

[26] N. Mahboob, H. Iqbal, M. Ahmed, M. M. H. Magnet, and K. Z. Mamun, “Disk diffusion Method in Enriched Mueller Hinton agar for determining susceptibility of Candida isolates from various clinical specimens,” *J. Dhaka Med. Coll.*, vol. 28, no. 1, pp. 28–33, 2020, doi: 10.3329/jdmc.v28i1.45753.

[27] S. K. Noukelag, L. C. Razanamahandry, S. K. O. Ntwampe, C. J. Arendse, and M. Maaza, "Industrial dye removal using bio-synthesised Ag-doped ZnO nanoparticles," *Environ. Nanotechnology, Monit. Manag.*, vol. 16, p. 100463, 2021, doi: https://doi.org/10.1016/j.enmm.2021.100463.

[28] S. Iqbal *et al.*, "Design Ag-doped ZnO heterostructure photocatalyst with sulfurised graphitic C3N4 showing enhanced photocatalytic activity," *Mater. Sci. Eng. B Solid-State Mater. Adv. Technol.*, vol. 272, no. September 2020, p. 115320, 2021, doi: 10.1016/j.mseb.2021.115320.

[29] H. Cai, Q. Qiao, S. Ren, D. Zhu, and Z. Xue, "Facile synthesis and photocatalytic performance of flowerlike Ag/ZnO nanocomposites," *Micro Nano Lett.*, vol. 13, no. 5, pp. 622–625, 2018, doi: 10.1049/mnl.2018.0019.

[30] B. Ramasamy, J. Jeyadharmarajan, and P. Chinnaiyan, “Novel organic assisted Ag-ZnO photocatalyst for atenolol and acetaminophen photocatalytic degradation under visible radiation: performance and reaction mechanism,” *Environ. Sci. Pollut. Res.*, vol. 28, no. 29, pp. 39637–39647, 2021, doi: 10.1007/s11356-021-13532-2.

[31] R. E. Adam *et al.*, “ZnO/Ag/Ag2WO4 photo-electrodes with plasmonic behavior for enhanced photoelectrochemical water oxidation,” *RSC Adv.*, vol. 9, no. 15, pp. 8271–8279, 2019, doi: 10.1039/c8ra10141h.

[32] S. R. Vijayalakshmidevi, S. Anju, and G. Melchias, “in Vitro Screening of C . Roseus Alkaloids for Antibacterial Activity,” *The Biosfile:///C:/Users/SENTHILKUMAR/Downloads/crystals-v12-i01_20220627.riscan*, vol. 6, no. 2, pp. 245–248, 2011.

[33] M. M. Ahmad, H. M. Kotb, S. Mushtaq, M. Waheed-Ur-rehman, C. M. Maghanga, and M. W. Alam, “Green Synthesis of Mn + Cu Bimetallic Nanoparticles Using Vinca rosea Extract and Their Antioxidant, Antibacterial, and Catalytic Activities,” *Crystals*, vol. 12, no. 1, 2022, doi: 10.3390/cryst12010072.

[34] P. Makvandi, C. yu Wang, E. N. Zare, A. Borzacchiello, L. na Niu, and F. R. Tay, “Metal-Based Nanomaterials in Biomedical Applications: Antimicrobial Activity and Cytotoxicity Aspects,” *Adv. Funct. Mater.*, vol. 30, no. 22, 2020, doi: 10.1002/adfm.201910021.

[35] T. A. Singh, J. Das, and P. C. Sil, “Zinc oxide nanoparticles: A comprehensive review on its synthesis, anticancer and drug delivery applications as well as health risks,” *Adv. Colloid Interface Sci.*, vol. 286, p. 102317, 2020, doi: https://doi.org/10.1016/j.cis.2020.102317.

[36] S. Chandrasekaran, V. Anbazhagan, and S. Anusuya, “Green route synthesis of ZnO nanoparticles using Senna auriculata aqueous flower extract as reducing agent and evaluation of its antimicrobial, antidiabetic and cytotoxic activity,” *Appl. Biochem. Biotechnol.*, 2022, doi: 10.1007/s12010-022-03900-0.